

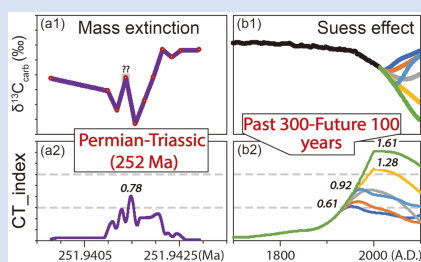
A novel carbon cycle turbulence index identifies environmental and ecological perturbations

Z.-H. Li¹, Z. Guo², Z.-Q. Chen^{2*}, S.W. Poulton^{1,3}, Y. Bao⁴,
L. Zhao^{1*}, F.-F. Zhang⁵

OPEN ACCESS

doi: 10.7185/geochemlet.2137

Abstract



Earth's history has been characterised by complex interactions between life and the environment, which are often difficult to resolve. Here, we propose a new carbon cycle turbulence index (CT_{index}), based on the carbonate-carbon isotope ($\delta^{13}C_{carb}$) record, to measure the extent of environmental perturbation over the last billion years. The CT_{index} trend is closely linked to Phanerozoic biotic extinction rates (ERs), as calculated from a palaeobiology database, supporting a strong environmental control on biotic ERs. We use the empirical CT_{index} —ER relationship to compare the extent of environmental perturbation due to greenhouse gas emissions with that during the Permian-Triassic (PTt) transition (~252 Ma), representing the most severe mass extinction of the Phanerozoic. At the current peak of fossil fuel emissions, the

CT_{index} indicates a moderate future environmental perturbation. However, if fossil fuel emissions increase into the next century, a pronounced CT_{index} peak greater than that which occurred during the PTt transition is indicated, which suggests the potential for a severe "sixth mass extinction" in the future.

Received 3 October 2021 | Accepted 6 December 2021 | Published 30 December 2021

Introduction

The evolution of life on Earth has been punctuated by extreme environmental/climatic events, often leading to mass extinctions (Chen and Benton, 2012; Rothman, 2017). Carbon cycle perturbations, global warming or cooling, and widespread anoxia have all played major roles in shaping the course of biotic macroevolution (Payne *et al.*, 2020). However, there is no general model that encompasses the range of scenarios documented by the geological record. For example, in terms of global $\delta^{13}C$ records, negative (*e.g.*, end Permian) and positive (*e.g.*, end Ordovician) excursions have both been linked to biotic extinctions (Fan *et al.*, 2020). Thus, while major biotic events were linked to intervals of environmental perturbation and ecologic disturbance, they were not universally driven by one particular environmental process. However, there are no reliable proxies for measuring the extent of carbon cycle instability and associated environmental stress through Earth history.

Here, we develop a carbon cycle turbulence index (CT_{index}) to measure perturbations in the $\delta^{13}C_{carb}$ record (Cramer and Jarvis, 2020) over the last 1,000 Myr. The CT_{index} emphasises perturbations to the carbon cycle as a metric for ecosystem instability. The rationale for using $\delta^{13}C_{carb}$ perturbation is because the $\delta^{13}C_{carb}$ record is robust and at high resolution, and short term

(0.5–10 Myr) $\delta^{13}C_{carb}$ variability over the past 1,000 Myr has been suggested to record ocean-atmosphere system instability (Rothman, 2017). The CT_{index} is calculated according to Equation 1:

$$CT_{index}(t) = \left(\frac{1}{N} \sum_{i=1}^N |F(i) - \mu(t)|^n \right)^{\frac{1}{n}} \quad (\text{Eq. 1})$$

To measure the degree of carbon cycle turbulence at each point ($CT_{index}(t)$), over a pre-determined duration (*e.g.*, $\tau_{span} = 0.05$ Myr), we compiled all the datum points within the τ_{span} (centred on the calculating point, t) in array F . In this case, N and $\mu(t)$ represent the number and average isotopic value of the array F , respectively, where n is a statistical control to avoid a situation where the sum of the mean deviations is zero. When $n = 2$, the output of the calculation, $CT_{index}(t)$, is equal to the standard deviation of the array F (see sensitivity tests for parameters τ_{span} and n in Supplementary Information). Thus, major positive and negative excursions will both result in a CT_{index} peak.

Phanerozoic biotic extinction rates (ERs) at the generic level were derived from a palaeobiology database (PaleoDB), and are applied to represent biodiversity changes and ecologic disturbance for comparison with CT_{index} values (Fig. 1). The fossil

1. State Key Laboratory of Geological Processes and Mineral Resources, China University of Geosciences, Wuhan 430074, China
2. State Key Laboratory of Biogeology and Environmental Geology, School of Earth Sciences, China University of Geosciences, Wuhan 430074, China
3. School of Earth and Environment, University of Leeds, Leeds, LS2 9JT, UK
4. Institute of Remote Sensing and Geographical Information Systems, School of Earth and Space Sciences, Peking University, Beijing, China
5. State Key Laboratory for Mineral Deposit Research, School of Earth Sciences and Engineering Frontiers Science Center for Critical Earth Material Cycling, Nanjing University, Nanjing 210023, China

* Corresponding author (email: zhong.qiang.chen@cug.edu.cn; lszhao@cug.edu.cn)



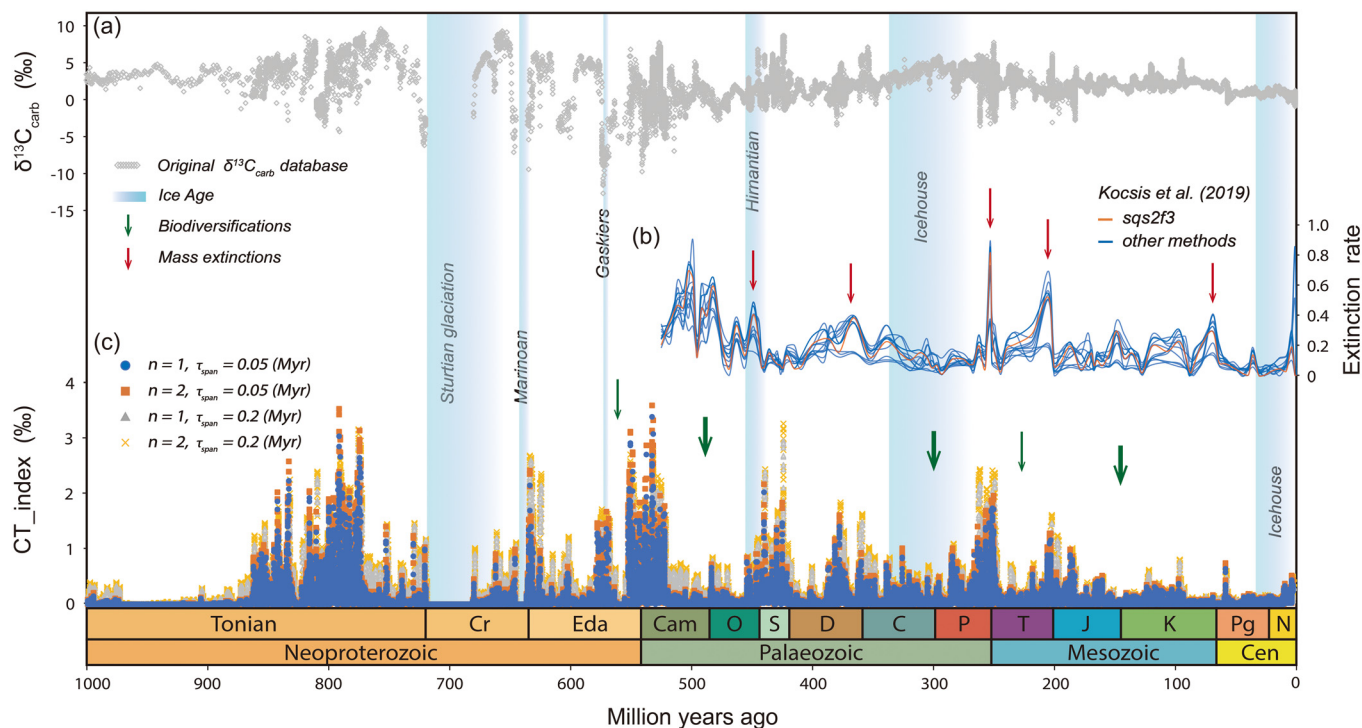


Figure 1 $\delta^{13}\text{C}_{\text{carb}}$ database (Cramer and Jarvis, 2020) and calculated CT_{index} values across the last 1,000 Myr, combined with calculated extinction rates through the Phanerozoic (from the paleobiology database; <http://www.paleobiodb.org/>; Kocsis et al., 2019).

record often documents a direct link between enhanced ERs and dramatic reductions in biodiversity, or major ecologic disturbance, during mass extinctions (Alroy et al., 2008). Hence, relationships between CT_{index} peaks and higher ER values can be employed to investigate coincidence between catastrophic environmental stress and biotic crises through Earth history. Moreover, increasing evidence suggests that we are in the midst of a “sixth mass extinction” (Barnosky et al., 2011; Ceballos et al., 2015), and a pronounced negative excursion in $\delta^{13}\text{C}_{\text{CO}_2}$ caused by greenhouse gas emissions has been recorded since the onset of the industrial revolution (Graven et al., 2020). In order to investigate the current and potential future significance of rising greenhouse gas emissions on biotic ERs, we compare the present day CT_{index} value to that observed during the Permian/Triassic (PTr) transition, representing the most severe mass extinction of the Phanerozoic.

Results and Discussion

CT_{index} vs. environmental perturbations. Our reconstruction of the CT_{index} through time (Fig. 1; analytical methods and database details are given in the Supplementary Information) highlights that it is both the magnitude and duration of the carbon cycle perturbation that exhibits a major link to the extent of environmental and biotic change. The CT_{index} offers a unique measure of the intensity of $\delta^{13}\text{C}_{\text{carb}}$ fluctuations, which reflect carbon cycle perturbation and the dynamic balance between the input of carbon and its burial as carbonate and organic matter (Kump and Arthur, 1999). As such, the CT_{index} peaks during the late Tonian, through the Cryogenian and Ediacaran glaciations, and into the Cambrian (Fig. 1), broadly correlate with periods of environmental oxygenation (Canfield et al., 2007; Lyons et al., 2021). The major variability evident in CT_{index} values (in both magnitude and frequency) reflects well documented instability in the extent of Earth surface oxygenation over this interval

(Canfield et al., 2008; Sahoo et al., 2016; He et al., 2019; Li et al., 2020).

As the Earth progressed to near modern levels of oxygenation in the Palaeozoic (Krause et al., 2018) and life continued to evolve and diversify (Lenton et al., 2016), the ensuing environmental stability generally resulted in lower peaks in CT_{index} values, with the exception of the major peak across the PTr boundary (Fig. 1). However, despite the general decrease, the CT_{index} trend is of sufficient resolution (see Fig. S-4) to distinguish nearly all of the major individual carbon cycle perturbations during the Phanerozoic (Fig. 1). Thus, although there are many potential controls on the $\delta^{13}\text{C}_{\text{carb}}$ record (Lenton et al., 2018), the CT_{index} provides an integrated and robust assessment of the overall extent of environmental perturbation.

Deciphering extinction rates and environmental perturbations. The CT_{index} trends correlate with biodiversity fluctuations, ERs and ecologic disturbance through the Neoproterozoic and Phanerozoic (Fig. 1). Several important intervals of biodiversification, including the initial evolution of the Ediacaran biota, the Cambrian explosion, the Great Ordovician Biodiversification, the Carboniferous-Permian, and the mid-Triassic and Jurassic-Cretaceous radiations (Sepkoski, 1981; Alroy et al., 2008; Erwin et al., 2011; Darroch et al., 2018; Fan et al., 2020), all coincide with low CT_{index} values. By contrast, pronounced CT_{index} peaks correspond to higher ERs, as evident during mass extinctions (Fig. 1b).

However, since the datum sampling densities of $\delta^{13}\text{C}_{\text{carb}}$ database and Paleodb are clearly different, it is difficult to directly calculate the regression relationship between the CT_{index} and ERs. To address this, we begin by identifying significant global perturbation events during the Phanerozoic (Fig. S-4, Table S-2). These 41 events comprise the major $\delta^{13}\text{C}_{\text{carb}}$ perturbations (Rothman, 2017), mass extinctions (Bambach, 2006), and biodiversifications (Fan et al., 2020). While the CT_{index} trend reflects the degree of environmental perturbation on the timescale of individual events (Fig. S-3), consideration needs to be

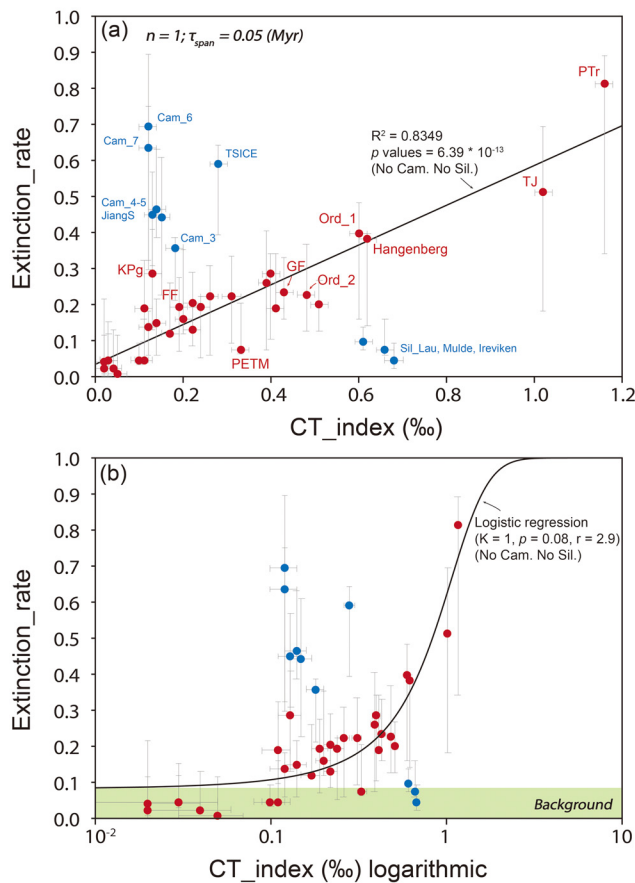


Figure 2 Cross plots of the extinction rate (ER) vs. the CT_{index} for 41 events. (a) Blue circles represent outlier events from the Cambrian and Silurian. Red circles represent the other events from the Phanerozoic, which show a strong correlation between ER and the CT_{index} . (b) Logarithmic plot of the extinction rate (ER) vs. the CT_{index} for 41 events, with the best fit logistic regression curve of the red circles. See Table S-2 for details.

given to the method for calculating ER ratios. Kocsis *et al.* (2019) explored 12 different metrics to calculate ER values (Fig. 1b), which also consider the potential errors caused by the PaleoDB itself. For each stage, we use the maximum, minimum and 'sqsf3' methods (Kocsis *et al.*, 2019) to establish a broad range for the calculation of ER values (Fig. 2, Fig. S-5). Then, each major CT_{index} peak is considered responsible for the corresponding ER perturbation.

Cross plots show that the CT_{index} and ER values for 31 of these events are broadly positively correlated (red points; Fig. 2), with $R^2 = 0.835$ and $p < 0.001$. The remaining 10 events (blue points; Fig. 2) comprise two types of outlier: (1) events with high ER and low CT_{index} values, occurring from 541 to 480 Ma (from the Cambrian to the first stage of the Ordovician), and (2) events with high CT_{index} and low ER values, occurring in Silurian. Given that the dataset for these latter two intervals is smaller than that of other periods of the Phanerozoic (Fig. S-4a), these outliers may result from the incompleteness of the PaleoDB. However, a fundamental difference in ecosystem stability for these periods, relative to the rest of the Phanerozoic, cannot be ruled out. Nevertheless, the CT_{index} suggests that environmental turbulence was intense during the early Cambrian (but not the middle to late Cambrian) and through the entire Silurian. While the high ER and low CT_{index} signal for 541–480 Ma may represent an unstable ecosystem, the high CT_{index} and low ER signal for

the Silurian reflects a more stable ecosystem that did not suffer a major extinction.

Next, in order to explore the potential thresholds of the mass extinctions, we use a logistic curve (sigmoid curve) to fit the data (Fig. 2b), which is a widely used approach for deep time extinction studies (Roopnarine, 2006). Logistic curves represent the battle between ecosystem stability and environmental instability. Ecosystems are generally unaffected at low levels of volatility, but when the degree of volatility increases to a certain threshold, the biotic ER rapidly increases (*e.g.*, the PTR and TJ mass extinctions).

In addition to distinguishing these well studied events, the logistic curve also provides new insight into broader trends through time. Here we note that a previous study of major $\delta^{13}C_{carb}$ events suggests that the thresholds of catastrophe in the Earth system have not changed systematically over time (Rothman, 2017). Building on this, our data implicitly suggest that, although life has evolved into more complex forms, ecosystem tolerance to environmental turbulence has not significantly improved through time (discounting the Cambrian and Silurian; Fig. S-5c). This observation naturally leads to consideration of whether the CT_{index} may be used to evaluate the possible nature of Earth's "sixth mass extinction" in the modern and future environment.

Contrasting the CT_{index} during the PTR and from 1700 to 2100 A.D. Current high extinction rates of some taxonomic groups suggest that the Earth may be entering a "sixth mass extinction", which may have a causal relationship with increasing greenhouse gases in the atmosphere (Barnosky *et al.*, 2011; Ceballos *et al.*, 2015). However, there is still a widely recognised "last kilometre gap" between the fossil record and the modern bio-record and their extinction rates, for the following reasons: (1) most modern data focus on terrestrial vertebrates (*e.g.*, mammals and birds), whereas the fossil record predominantly reflects marine invertebrates (*e.g.*, brachiopods, gastropods and bivalves) (Kocsis *et al.*, 2019), and (2) there are different time spans when considering a particular extinction. Specifically, the "Big Five" Phanerozoic mass extinctions are only constrained across a broad time resolution of millions of years, so a comparison with modern events occurring on a timescale of a hundred to a thousand years is not straightforward, and (3) there is uncertainty in the near future. For example, calculation of ERs for modern species is hampered since it remains unknown whether "critically endangered species" will actually go extinct (Barnosky *et al.*, 2011). (4) Other unknowns, including continental configuration, pre-existing climate state, and the extant biota at the time of CT_{index} perturbation might also affect how the ER responds.

To address these issues, we note that if the core hypothesis of the CT_{index} stands, then the sixth mass extinction should be accompanied by a distinct CT_{index} peak. We thus reconstruct CT_{index} values from 1700 to 2100 A.D., representing the time period prior to, and after, the industrial revolution, and we contrast this with the PTR transition at ~252 Ma, representing the most severe mass extinction of the Phanerozoic. We used $\delta^{13}CO_2$ curves from ice core to reconstruct the modern CT_{index} trend due to its complete and robust record over the last several centuries, in addition to the availability of modelled near future values (Rubino *et al.*, 2013; Graven *et al.*, 2020). However, we note that other carbon hosts, including surface ocean dissolved inorganic carbon, coral samples, and CH_4 in Antarctica ice core also sensitively record significant CT_{index} peaks (Fig. S-7). This approach is reinforced by an observed strong similarity in the CT_{index} output when calculated using the $\delta^{13}CO_2$ and $\delta^{13}C$ coral records (Fig. S-7). To further enhance the reliability of our comparison, we focus on a very short interval during the PTR

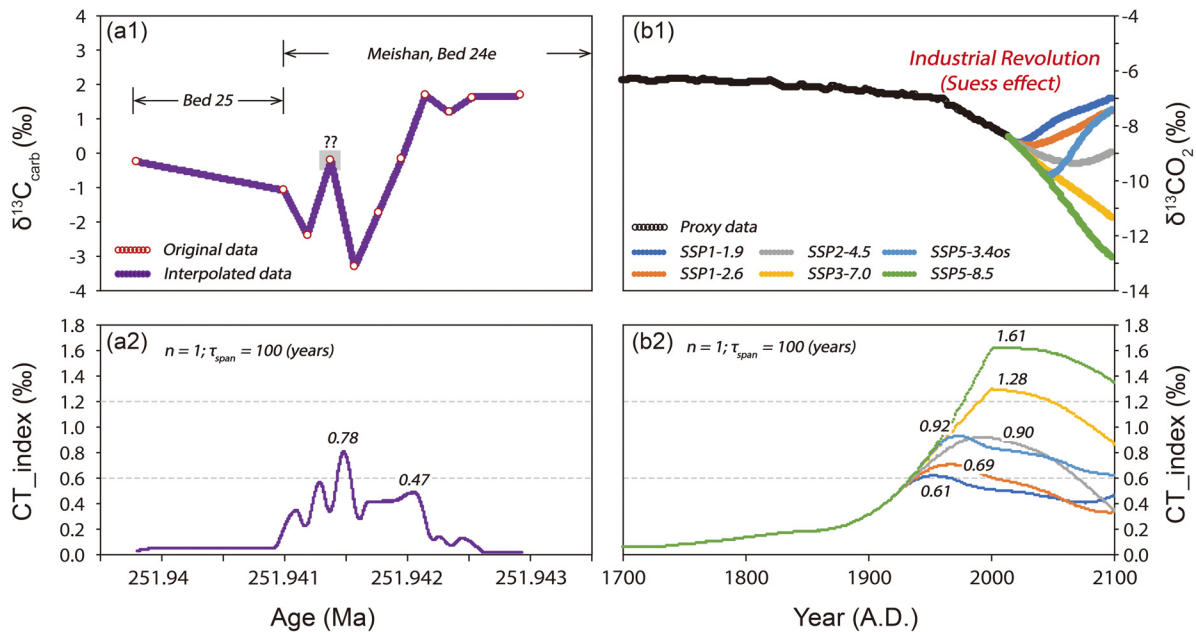


Figure 3 Comparison of $\delta^{13}\text{C}_{\text{carb}}$ and $\delta^{13}\text{CO}_2$ across the PTR mass extinction and the Industrial Revolution period, and the calculated CT_{index} . **(a)** PTR dataset collected from bed 24e to 25, Meishan section (Burgess *et al.*, 2014). **(b)** Industrial Revolution period (Rubino *et al.*, 2013). The future $\delta^{13}\text{CO}_2$ estimations are based on CMIP6 Scenario-MIP (Graven *et al.*, 2020). All the original data were interpolated to a one point per year resolution; $\tau_{\text{span}} = 0.0001$ Ma (100 year) and $n = 1$ were employed to run the CT_{index} .

transition, between Bed 24e to Bed 25 in the Meishan GSSP section, which documents the extinction level itself (Burgess *et al.*, 2014). This interval has 11 original $\delta^{13}\text{C}_{\text{carb}}$ datum points across an estimated interval of $\sim 3,000$ years. Hence, we calculate the CT_{index} for both the PTR and the industrial revolution period using the same parameters ($n = 1$; $\tau_{\text{span}} = 100$ years), and the datasets were pre-normalised to a datum density of one point per year.

The relative size of the CT_{index} peaks calculated under the same conditions for the two time intervals is of practical comparative significance (Fig. 3). The CT_{index} peak during the PTR ranges from 0.47 to 0.78, whilst the CT_{index} peak of the industrial revolution period ranges from 0.61 to 1.61, with the latter reflecting the predicted range for the $\delta^{13}\text{CO}_2$ trend into the near future. If fossil fuel emissions peak at the present level and are at a low level through the next century, it has been suggested (Graven *et al.*, 2020) that $\delta^{13}\text{CO}_2$ may recover from -8.8 ‰ to 7.0 ‰, which leads to a moderate CT_{index} peak (line SSP1-1.9; Fig. 3). However, in other scenarios without such effective limits on fossil fuel emissions, $\delta^{13}\text{CO}_2$ will likely continue to decrease through the next century (line SSP8.5), causing a dramatic peak in the CT_{index} that may be even greater than the PTR CT_{index} peak (Fig. 3). While the current extinction of species is driven by biodiversity loss that is only partly associated with fossil fuel driven climate change, the empirical relationship between ecosystem stability and biotic ERs implies that, if fossil fuel emissions are not significantly decreased, Earth's "sixth mass extinction" has the potential to be severe.

Acknowledgements

The contributors to the PaleoDB database and Geologic Time Scale are thanked for their provision of taxonomic and carbon isotope data for the database. We are grateful to Gavin Foster and two anonymous reviewers for their comments, which greatly improved this manuscript. This study was supported by five NSFC grants (41821001, 41930322, 41977264, 42073002,

92055212), and by 111 Project of China (BP0820004). ZL is funded by the Fundamental Research Funds for National Universities, China University of Geosciences (Wuhan).

Editor: Gavin Foster

Additional Information

Supplementary Information accompanies this letter at <https://www.geochemicalperspectivesletters.org/article2137>.



© 2021 The Authors. This work is distributed under the Creative Commons Attribution Non-Commercial No-Derivatives 4.0

License, which permits unrestricted distribution provided the original author and source are credited. The material may not be adapted (remixed, transformed or built upon) or used for commercial purposes without written permission from the author. Additional information is available at <https://www.geochemicalperspectivesletters.org/copyright-and-permissions>.

Cite this letter as: Li, Z.-H., Guo, Z., Chen, Z.-Q., Poulton, S.W., Bao, Y., Zhao, L., Zhang, F.-F. (2021) A novel carbon cycle turbulence index identifies environmental and ecological perturbations. *Geochim. Persp. Let.* 20, 11–15.

References

- ALROY, J., ABERHAN, M., BOTTJER, D., FOOTE, M., FURSICH, F.T., HARRIES, P.J., HENDY, A.J.W., HOLLAND, S.M., LVANY, L.C., KIESSLING, W., KOSNIK, M.A., MARSHALL, C.R., MCGOWAN, A.J., MILLER, A.I., OLSZEWSKI, T.D., PATZKOWSKY, M.E., PETERS, S.E., VILLIER, L., WAGNER, P.J., BONUSO, N., BORKOW, P.S., BRENNES, B., CLAPHAM, M.E., FALL, L.M., FERGUSON, C.A., HANSON, V.L., KRUG, A.Z., LAYOU, K.M., LECKEY, E.H., NURNBERG, S., POWERS, C.M., SESSA, J.A., SIMPSON, C., TOMASOVYCH, A., VISAGGI, C.C. (2008) Phanerozoic Trends in the Global Diversity of Marine Invertebrates. *Science* 321, 97–100.
- BAMBACH, R.K. (2006) Phanerozoic Biodiversity Mass Extinctions. *Annual Review of Earth and Planetary Sciences* 34, 127–155.



- BARNOSKY, A.D., MAITZKE, N., TOMIYA, S., WOGAN, G.O.U., SWARTZ, B., QUENTAL, T.B., MARSHALL, C., MCGUIRE, J.L., LINDSEY, E., MAGUIRE, K.C., MERSEY, B., FERRER, E.A. (2011) Has the Earth's sixth mass extinction already arrived? *Nature* 471, 51–57.
- BURGESS, S.D., BOWRING, S., SHEN, S. (2014) High-precision timeline for Earth's most severe extinction. *PNAS* 111, 3316–3321.
- CANFIELD, D.E., POULTON, S.W., NARBONNE, G.M. (2007) Late-Neoproterozoic Deep-Ocean Oxygenation and the Rise of Animal Life. *Science*, New Series 315, 92–95.
- CANFIELD, D.E., POULTON, S.W., KNOLL, A.H., NARBONNE, G.M., ROSS, G., GOLDBERG, T., STRAUSS, H. (2008) Ferruginous Conditions Dominated Later Neoproterozoic Deep-Water Chemistry. *Science* 321, 949–952.
- CEBALLOS, G., EHRLICH, P.R., BARNOSKY, A.D., GARCÍA, A., PRINGLE, R.M., PALMER, T.M. (2015) Accelerated modern human-induced species losses: Entering the sixth mass extinction. *Science Advances* 1, e1400253.
- CHEN, Z.-Q., BENTON, M.J. (2012) The timing and pattern of biotic recovery following the end-Permian mass extinction. *Nature Geoscience* 5, 375–383.
- CRAMER, B.D., JARVIS, I. (2020) Chapter 11 - Carbon Isotope Stratigraphy. In: GRADSTEIN, F.M., OGG, J.G., SCHMITZ, M.D., OGG, G.M. (Eds.) *The Geologic Time Scale 2020*. Elsevier, Amsterdam, 309–343. doi: [10.1016/B978-0-12-824360-2.00011-5](https://doi.org/10.1016/B978-0-12-824360-2.00011-5).
- DARROCH, S.A.F., SMITH, E.F., LAFLAMME, M., ERWIN, D.H. (2018) Ediacaran Extinction and Cambrian Explosion. *Trends in Ecology & Evolution* 33, 653–663.
- ERWIN, D.H., LAFLAMME, M., TWEEDT, S.M., SPERLING, E.A., PISANI, D., PETERSON, K.J. (2011) The Cambrian Conundrum: Early Divergence and Later Ecological Success in the Early History of Animals. *Science* 334, 1091–1097.
- FAN, J.X., SHEN, S.Z., ERWIN, D.H., SADLER, P.M., MACLEOD, N., CHENG, Q.M., HOU, X.D., YANG, J., WANG, X.D., WANG, Y., ZHANG, H., CHEN, X., LI, G.X., ZHANG, Y.C., SHI, Y.K., YUAN, D.X., CHEN, Q., ZHANG, L.N., LI, C., ZHAO, Y.Y. (2020) A high-resolution summary of Cambrian to Early Triassic marine invertebrate biodiversity. *Science* 367, 272–277.
- GRAVEN, H., KEELING, R.F., ROGELJ, J. (2020) Changes to Carbon Isotopes in Atmospheric CO₂ Over the Industrial Era and Into the Future. *Global Biogeochemical Cycles* 34, e2019GB006170.
- HE, T.C., ZHU, M.Y., MILLS, B.J.W., WYNN, P.M., ZHURAVLEV, A.Y., TOSTEVIN, R., POGGE VON STRANDMANN, P.A.E., YANG, A.H., POULTON, S.W., SHIELDS, G.A. (2019) Possible links between extreme oxygen perturbations and the Cambrian radiation of animals. *Nature Geoscience* 12, 468–474.
- KOCSIS, A.T., REDDIN, C.J., ALROY, J., KIESSLING, W. (2019) The r package divDyn for quantifying diversity dynamics using fossil sampling data. *Methods in Ecology and Evolution* 10, 735–743.
- KRAUSE, A.J., MILLS, B.J.W., ZHANG, S., PLANAVSKY, N.J., LENTON, T.M., POULTON, S.W. (2018) Stepwise oxygenation of the Paleozoic atmosphere. *Nature Communications* 9, 4081.
- KUMP, L.R., ARTHUR, M.A. (1999) Interpreting carbon-isotope excursions: carbonates and organic matter. *Chemical Geology* 161, 181–198.
- LENTON, T.M., DAINES, S.J. (2018) The effects of marine eukaryote evolution on phosphorus, carbon and oxygen cycling across the Proterozoic–Phanerozoic transition. *Emerging Topics in Life Sciences* 2, 267–278.
- LENTON, T.M., DAHL, T.W., DAINES, S.J., MILLS, B.J.W., OZAKI, K., SALTZMAN, M.R., PORADA, P. (2016) Earliest land plants created modern levels of atmospheric oxygen. *PNAS* 113, 9704–9709.
- LI, Z., CAO, M., LOYD, S.J., ALGEO, T.J., ZHAO, H., WANG, X., ZHAO, L., CHEN, Z.-Q. (2020) Transient and stepwise ocean oxygenation during the late Ediacaran Shuram Excursion: Insights from carbonate $\delta^{238}\text{U}$ of northwestern Mexico. *Precambrian Research* 344, 105741.
- LYONS, T.W., DIAMOND, C.W., PLANAVSKY, N.J., REINHARD, C.T., LI, C. (2021) Oxygenation, Life, and the Planetary System during Earth's Middle History: An Overview. *Astrobiology* 21, 906–923.
- PAYNE, J.L., BACHAN, A., HEIM, N.A., HULL, P.M., KNOPE, M.L. (2020) The evolution of complex life and the stabilization of the Earth system. *Interface Focus* 10, 20190106.
- ROOPNARINE, P.D. (2006) Extinction cascades and catastrophe in ancient food webs. *Paleobiology* 32, 1–19.
- ROTHMAN, D.H. (2017) Thresholds of catastrophe in the Earth system. *Science Advances* 3, e1700906.
- RUBINO, M., ETHERIDGE, D.M., TRUDINGER, C.M., ALLISON, C.E., BATTLE, M.O., LANGENFELDS, R.L., STEELE, L.P., CURRAN, M., BENDER, M., WHITE, J.W.C., JENK, T.M., BLUNIER, T., FRANCEY, R.T. (2013) A revised 1000 year atmospheric $\delta^{13}\text{C}$ -CO₂ record from Law Dome and South Pole, Antarctica. *Journal of Geophysical Research: Atmospheres* 118, 8482–8499.
- SAHOO, S.K., PLANAVSKY, N.J., JIANG, G., KENDALL, B., OWENS, J.D., WANG, X., SHI, X., ANBAR, A.D., LYONS, T.W. (2016) Oceanic oxygenation events in the anoxic Ediacaran ocean. *Geobiology* 14, 457–468.
- SEPKOSKI, J.J. (1981) A factor analytic description of the Phanerozoic marine fossil record. *Paleobiology* 7, 36–53.



A novel carbon cycle turbulence index identifies environmental and ecological perturbations

Z.-H. Li, Z. Guo, Z.-Q. Chen, S.W. Poulton, Y. Bao,
L. Zhao, F.-F. Zhang

Supplementary Information

The Supplementary Information includes:

- The Geochemical and Paleobiology Databases
- Analytical Approaches and Statistical Analysis
- Datum Density vs. Bias
- Comparison of Carbon Cycle Perturbations and CTindex Values between the Permian-Triassic Mass Extinction and the Industrial Revolution Period of the Anthropocene
- Tables S-1 and S-2
- Figures S-1 to S-8
- Supplementary Information References

The Geochemical and Paleobiology Databases

The carbon isotope ($\delta^{13}\text{C}_{\text{carb}}$) dataset through the last one billion years is adapted from [Cramer and Jarvis \(2020\)](#) and collected from other key studies ([Xiao *et al.*, 2014](#); [Zhu *et al.*, 2019](#); [Rooney *et al.*, 2020](#); [Westerhold *et al.*, 2020](#)). We note that $\delta^{13}\text{C}_{\text{carb}}$ data before and after ~650 Ma have markedly different data density ([Fig. S-1](#)), with the ~1000 to 650 Ma period having lower density and intervals with no data. However, this feature does not affect the analyses focused on the Phanerozoic.

The Sepkoski database (Sepkoski, 1996) and Paleobiology database (PaleoDB, <http://www.paleobiodb.org/>, <http://fossilworks.org>) are employed to calculate biotic extinction rates at the genus level through the Phanerozoic. The former was only used as a comparison in Figure S-2, while the latter was used to run the CT_{index} curves. It should be noted that the raw dataset (PaleoDB) that was used in this study follows Kocsis *et al.* (2019), which was downloaded on May 31, 2019 (https://github.com/divDyn/ddPhanero/raw/master/data/PaleoDB/2019-05-31_paleoDB.RData). Time series were drafted based on the resolution of Stages (Ages), which is the highest resolution of the PaleoDB. Twelve different metrics (Fig. 1b) were set to calculate ER based on three different data treatments, including: raw data, Classical Rarefaction (cr), and Shareholder Quorum Subsampling (sqs). In addition, four different rate calculation methods were employed, including: per capita rates, corrected three-timer rates, gap-filler equations, and second-for-third substitution rates. Kocsis *et al.* (2019) suggested metric, with sqs data treatment and second-for-third substitution rates ('sqs2f3'), should be used as the standard extinction rate trend in this study. The other metrics were used as a necessary contrast to form the error bars in Figure 2.

Analytical Approaches and Statistical Analysis

All mathematical approaches were performed in R (for the PaleoDB) and Matlab (other processes). The original $\delta^{13}\text{C}_{\text{carb}}$ database has an uneven sample resolution across different intervals. We used an interpolation method to average all densities to 0.02 Ma per point (Fig. S-1), which is employed in Matlab by using the function 'interp1' with method 'Linear'. In particular, the original $\delta^{13}\text{C}_{\text{carb}}$ database (Westerhold *et al.*, 2020) has a much higher resolution from 0 to 0.5 Ma (~0.005 Ma per point), whilst the resolution from 750 to 2100 A.D. is ~1 year per point. For these higher resolution intervals, we did not lower the resolution to be consistent with more ancient intervals. The CT_{index} value therefore reflects $\delta^{13}\text{C}_{\text{carb}}$ variability not only on a long-timescale (>10 Ma), but also within a short-timescale (>0.02 Ma). Multiple studies have suggested that $\delta^{13}\text{C}_{\text{carb}}$ may dominantly reflect the original ocean-atmosphere carbon isotope composition and can sensitively record oscillations across this short-timescale (Bachan *et al.*, 2017), although local restriction, water-mass ageing and authigenic carbonate formation may also affect the isotopic record (Swart, 2008). The CT_{index} , however, weakens the direction or simple magnitude of $\delta^{13}\text{C}_{\text{carb}}$ excursions and emphasises the possibility of isotopic instability over a predetermined timespan (see sensitivity test in Fig. S-3 for further detail).

The post-interpolation $\delta^{13}\text{C}_{\text{carb}}$ dataset was used to calculate the CT_{index} according to Equation 1. And the number of datum points within a predetermined τ_{span} should be kept the same to ensure that the calculation of

CT_{index} is not affected by different datum densities across different time periods. Given the fact that differentiation between the parameters τ_{span} and n will significantly shift the output of the calculation, we employed sensitivity analyses of τ_{span} and n to the CT_{index} (Fig. 1), indicating that as both τ_{span} and n increase, the output of the CT_{index} also increases synchronously. However, when the datum density is high (e.g., PTR interval and Cenozoic), there is little deviation when these parameters change (differentiation <10 %). We note here that the parameter τ_{span} plays a more important role in running CT_{index} , and thus dependent on the τ_{span} used, a very different CT_{index} value may be obtained. As shown in Figure S-3, we used some simple ‘witches hat’ pulses (linear increase followed by linear decline at the same rate), and the time-dependent forcing pulses for $\delta^{13}\text{C}_{\text{carb}}$ variations are given in Equations S-1-3:

$$\text{Pulse}_1 = [0:0.1:1.2], [0 \ 0 \ 5 \ 0 \ 0 \ -5 \ 0 \ 0 \ 5 \ 0 \ 0 \ 5 \ 0] \quad (\text{Eq. S-1})$$

$$\text{Pulse}_2 = [0 \ 0.4 \ 0.5 \ 0.6 \ 1.2], [0 \ 0 \ 5 \ 0 \ 0] \quad (\text{Eq. S-2})$$

$$\text{Pulse}_3 = [0 \ 0.4 \ 0.6 \ 0.7 \ 0.9 \ 1.2], [0 \ 0 \ 7 \ 7 \ 0 \ 0] \quad (\text{Eq. S-3})$$

where the first vectors are time (in Myrs) and the second vectors are the $\delta^{13}\text{C}_{\text{carb}}$ values (in ‰). Different τ_{span} values were used for a sensitivity test. Rothman (2017) observed that the duration of the major carbon isotope events through the entire Phanerozoic is approximately limited between 10^4 to 10^6 years. This means that if we employ a longer (larger) τ_{span} (e.g., $\tau_{\text{span}} \geq 1$ Ma), the CT_{index} is unable to distinguish individual events, and the CT_{index} curve would represent a mixed signal of adjacent events (Fig. S-3a). This feature is directly evidenced by Pulse_1, which also shows that the CT_{index} is not sensitive to the direction of the carbon isotope excursion. In addition, multiple carbon isotope events have different degrees of offset and duration (simplified as Pulse_2 and Pulse_3). When τ_{span} is greater than the event duration, calculated CT_{index} values and the timing of the CT_{index} perturbation are not accurate (Fig. S-3b). When τ_{span} greatly exceeds the event duration, CT_{index} values approach a straight line with artificially high values (Fig. S-3b). Hence, the τ_{span} value may be greater than the events of relatively small duration (e.g., PTR) and lower than the events of relatively large duration (e.g., SPICE). In this case, we suggest to employ a relatively low τ_{span} , which should be similar to the minimum duration of the events in question (e.g., the duration of the PTR = ~0.06 Ma, and the duration of the PETM = ~0.08 Ma). In this case, a τ_{span} of 0.05 Ma is our recommended standard value, which is greater than the average density (= 0.02 Ma per point) of the $\delta^{13}\text{C}_{\text{carb}}$ database, but less than the more short-lived intervals of interest. The parameter τ_{span} may still be accurate (but smaller) if the resolution of carbon isotopes is further

improved. For instance, we employ a τ_{span} of 0.0001 Ma (100 years) for our subsequent evaluation of the interval from 700-2100 A.D.

In order to reveal the relationship between CT_{index} and ER, we employed a logistic function to test the data of 41 events (Eq. S-4):

$$P(x) = \frac{K * P_0 * e^{rx}}{K + P_0 * (e^{rx} - 1)} \quad (\text{Eq. S-4})$$

which calculates the logistic curve (sigmoid curve) and is used to run the logistic regression, where x denotes the CT_{index} , and $P(x)$ denotes the calculated ER. P_0 and K represent background ER and maximum ER values, respectively, and r is a free parameter measuring how fast the curve varies. When the CT_{index} is infinite, ER is equal to $K = 1$, indicating that all organisms became extinct. A logistic function was fitted to the data (Fig. 2). All the datum points contributing to Figure 3 are listed in Table S-2. When CT_{index} approaches zero indefinitely, the $\text{ER} = \sim 0.086$.

In order to reveal the similar statistical distribution of the CT_{index} and biotic extinction rates, we employed a log-normal distribution function to test the original databases (Eq. S-5):

$$\phi \ln(x) = \frac{1}{\sqrt{2\pi} * \delta x} \exp\left(-\frac{(\ln x - \mu)^2}{2\delta^2}\right) \quad (\text{Eq. S-5})$$

$$E(X) = e^{\mu + \delta^2/2} \quad (\text{Eq. S-6})$$

$$\text{var}(X) = (e^{\delta^2} - 1) * e^{2\mu + \delta^2} \quad (\text{Eq. S-7})$$

where x denotes that the CT_{index} and generic ER are a random variable. Both μ and σ are free parameters in this distribution function, which are the mean and standard deviation of logarithms of variables, respectively. The mathematic expectation ($E(X)$) and variance ($\text{var}(X)$) were calculated by Equations S-6 and S-7, respectively. The histograms of the $\delta^{13}\text{C}_{\text{carb}}$ and ER values fit with log-normal distribution functions (Fig. S-2, Table S-1). The CT_{index} values since the mid-Tonian are divided into two parts: 870-520 Ma and 520-0 Ma. The log-normal best fit curves of the histogram show that the CT_{index} values prior to 520 Ma ($E(X) = 0.246$) are relatively higher than afterwards ($E(X) = 0.168$), implying more volatility in the carbon cycle from 860 to 520 Ma. However, we note that there are some $\delta^{13}\text{C}_{\text{carb}}$ data gaps and this reduces the accuracy of CT_{index} output during the Precambrian period.



Datum Density vs. Bias

The $\delta^{13}\text{C}_{\text{carb}}$ database and PaleoDB covering the entire Phanerozoic were used to calculate the CT_{index} and ER values, respectively. The uneven density distribution in the datasets is a major potential source of the error when calculating both the CT_{index} and the ER. As shown in [Fig. S-1b](#), the density of the $\delta^{13}\text{C}_{\text{carb}}$ database is lower than 0.05 Ma per point, except for some intervals of high density. Therefore, we have uniformly pre-normalised the density of the $\delta^{13}\text{C}_{\text{carb}}$ database to 0.02 Ma per point.

The PaleoDB has a different and more complex sampling density to the $\delta^{13}\text{C}_{\text{carb}}$ database. The density of Stage (or substage) time-bin is lower than that of the $\delta^{13}\text{C}_{\text{carb}}$ database. Following the [Sepkoski \(1996\)](#) scheme, each stage has three statistical points corresponding to the start, middle and end ages. The calculated ER has the age point set to the middle age of each stage/substage. For instance, the Induan (early Triassic) contains three statistical age points calibrated to 251.9, 251.6 and 251.2 Ma. The ER of the Induan was calculated based on extinction rate data from the middle age point (251.6 Ma), and its value is 0.5, then the ER and its age for the Induan are expressed as [0.5, 251.6]. This differentiation of density causes potential error when calculating the correlation between CT_{index} and ERs ([Fig. S-4](#)), because the resolution of this three-statistical-points scheme is much lower than that of the CT_{index} curve, and the major CT_{index} peaks in each stage may not exactly emerge at the three-statistical-points of this stage. For instance, the onset timing of the PTr carbon isotope excursion is ~251.94 Ma, which is apparently not at the three-statistical-points of the Changhsingian. To minimise this bias, we assume that the onset timing of the major extinction events is equal to the onset timing of the major carbon isotope excursion in each stage. In other words, the ER curves have a normalised new timing abscissa, as listed in [Table S-2](#).

In terms of the taxonomic data of the PaleoDB, the uneven collections and/or occurrences will lead to different degrees of data quality between different stages. Specifically, the periods including the early Cambrian, Silurian, and Stages Bashkirian, Kasimovian and Thanetian, are characterised by extremely low collections (red boxes, [Fig. S-4a](#)). This will likely make the calculated ERs less reliable, and for these five low-quality data intervals special attention was paid in the following CT_{index} and ER correlation processes.

The PTr and TJ intervals have nearly an order of magnitude higher CT_{index} and ERs than other events, and this can cause the correlation between them to be artificially high. Hence, the CT_{index} and ER values are logarithmic normalised to eliminate the effect of order of magnitude differences in correlation. As shown in [Fig. S-5b](#),



after the logarithmic normalisation, the relationship between the CT_{index} and ER remains highly relevant ($R^2 = 0.697$, p values = $5.21 * 10^{-9}$).

Furthermore, positive correlations are also observed between the ER of various clades (phylum or class) and CT_{index} values during these events (Fig. S-5d), where the slopes of the ER- CT_{index} represent the tolerance of animal genera to environmental perturbation, indicating that the precise behavior of each clade is different when the CT_{index} value increases. Specifically, the Cnidaria, Brachiopoda and Cephalopoda suffered more severe extinctions (higher ER- CT_{index} slopes) relative to the Arthropoda, Bivalvia and Gastropoda. This indicates that the Cnidaria were physiologically fragile and more unbuffered, and the other clades were less affected and more physiologically buffered, strengthening observations on the decrease in physiologically unbuffered taxa and increase in physiologically buffered taxa after the PTr extinction (Knoll *et al.*, 2007; Payne *et al.*, 2020).

Comparison of Carbon Cycle Perturbations and CT_{index} Values between the Permian-Triassic Mass Extinction and the Industrial Revolution Period of the Anthropocene

We highlight carbon perturbations and CT_{index} values across two critical periods, represented by the most severe mass extinction of the Phanerozoic, and the last ~300 years before and after the Industrial Revolution (Suess effect). Both periods record high greenhouse gas emissions and pronounced negative excursions in $\delta^{13}C_{carb}$.

In the original $\delta^{13}C_{carb}$ database, data for the PTr period is proxied by the GSSP Meishan section (Burgess *et al.*, 2014). To provide a more detailed case study, we compiled C isotope data for another three well-studied sections around the palaeo-Tethys realm, including: Zal (Iran, Zhang *et al.*, 2018), Bálvány North (Hungary, Schobben *et al.*, 2017), and Wadi Shahha (Arabian, Clarkson *et al.*, 2013). During the PTr, data density is higher than in other geologic intervals, reaching $\sim 10^{-4}$ Ma per point. Hence, we employed $\tau_{span} = 0.05$ and 0.01 to run the CT_{index} . Fig. S-6 shows that due to the $\delta^{13}C_{carb}$ excursion, the CT_{index} abruptly reaches 1.2 to 1.6 in Meishan, with relatively high values in the other sections, indicating that the huge carbon cycle perturbation was clearly recorded around the entire palaeo-Tethys. With an ER of ~ 0.81 (Fan *et al.*, 2020), the PTr is distinguished from the other events on a cross plot of ER vs CT_{index} (Fig. 2). However, the datum resolution of the PTr event still has an unbridgeable gap relative to the modern carbon isotope record. Hence, we focus



on an extremely short period containing 11 data points from bed 24e to bed 25 of the Meishan section. This period represents a duration of ~3000 years (Burgess *et al.*, 2014), and is characterised by a significant sharp $\delta^{13}\text{C}_{\text{carb}}$ excursion, whilst the carbon isotope data were subjected to an Interpolation method to achieve one point per year data resolution (Fig. 3). Then a comparison can be employed between the PTr and the Industrial Revolution period across the same event duration and τ_{span} .

In terms of the Industrial Revolution period, we compiled $\delta^{13}\text{CO}_2$ data from 700 to 2100 A.D. (Rubino *et al.*, 2013; Bauska *et al.*, 2015; Graven *et al.*, 2020). For the geologic record we used carbonate carbon isotopes, but for the Industrial Revolution period we used atmospheric CO_2 carbon isotopes. While the carbon isotope signatures from these different sources have different triggering mechanisms and observations, they should result in only a minor difference in the final CT_{index} values. For example, for coral carbon isotope records around the world, the average declining rate = -0.022 ‰ per year from 1960 to 2000 A.D. (Liu *et al.*, 2021); for the globally averaged $\delta^{13}\text{C}$ -DIC (dissolved inorganic carbon) at the sea-surface, the declining rate = -0.013 ‰ per year from 1960 to 2000 A.D. (Kwon *et al.*, 2021); for $\delta^{13}\text{CO}_2$ in ice core the declining rate = -0.025 ‰ per year from 1960 to 2000 A.D. (Rubino *et al.*, 2013). These carbon carriers all record the ‘Suess effect’, which is a dilution effect whereby burning of fossil fuels increases $^{12}\text{CO}_2$ at a faster relative rate than $^{13}\text{CO}_2$ and $^{14}\text{CO}_2$ (Suess, 1955). For the $\delta^{13}\text{C}$ composition of CH_4 in Antarctica ice core, the increasing rate = 0.024 ‰ per year from 1960 to 2000 A.D. (Mischler *et al.*, 2009), which is caused by biomass burning being closely related to the agricultural source scales and population. The calculated CT_{index} curves for these four carbon carriers are plotted in Figure S-7. All four carriers show peaks of the same order of magnitude as during the PTr. It should be noted that the $\delta^{13}\text{C}$ -coral records (orange lines) and $\delta^{13}\text{CO}_2$ (yellow lines) have totally different carbon isotopic values and shifts, but they show nearly the same CT_{index} curves, demonstrating that from the point of view of the CT_{index} , the $\delta^{13}\text{CO}_2$ record can be directly compared to the $\delta^{13}\text{C}$ -coral record, and hence the palaeo- $\delta^{13}\text{C}_{\text{carb}}$ record.

The near future data in Figure S-8 were predicted by using six scenarios based on the shared socioeconomic pathways (SSPs) from the 6th Coupled Model Intercomparing Project (CMIP6) (Graven *et al.*, 2020), with each scenario having a profound influence on the determination of the CT_{index} . If $\delta^{13}\text{CO}_2$ peaks in the near future and falls back quickly, the CT_{index} will be limited to a much lower value, but if $\delta^{13}\text{CO}_2$ keeps falling, the ‘Suess effect’ may create a larger and sharper carbon isotope excursion than the PTr, resulting in a major CT_{index} peak. A τ_{span} of 0.05 Ma was used to calculate the Industrial Revolution period CT_{index} data, in order to compare to the deep-time data resolution. However, as discussed in relation to the τ_{span} sensitivity test (Fig.



S-3), when τ_{span} is a significantly larger than the duration of the event, the CT_{index} approaches a straight line and represents a mixed signal within the time span. Hence, we keep all the variables (or parameters) at the same values to compare the PTr and Industrial Revolution periods. Since the time resolution of the Industrial Revolution is much higher than that of the PTr, we employed $\tau_{\text{span}} = 0.0001$ Ma (100 year) and $n = 1$ to run the CT_{index} of both PTr (251.94 to 251.942 Ma) and Industrial Revolution (1700 to 2100 A.D.) periods, and the resolution of the datasets were set to equal to one point per one year by employing the function ‘`interp1`’ with method ‘`Linear`’ in Matlab.



Supplementary Tables

Table S-1 The best-fit parameters of the log-normal function fitted to the histograms.

| | CT_index | | Extinction rate | |
|----------|--------------|------------|-----------------|-----------------------------|
| | 520 - 860 Ma | 0 - 520 Ma | Sepkoski (1996) | Kocsis <i>et al.</i> (2019) |
| μ | -3.563 | -3.228 | -1.906 | -1.998 |
| δ | 1.887 | 1.912 | 0.837 | 1.013 |
| E(X) | 0.168 | 0.246 | 0.211 | 0.226 |
| var(X) | 0.964 | 2.284 | 0.045 | 0.092 |



Table S-2 Event names, event intervals (stages and ages) and data used to construct Figures 2 and S-5. B. = background, representing stabilised and diversification intervals with extremely low ER and CT_{index} values. These events are timed by biostratigraphy with reference to the Geologic Time Scale (Cramer and Jarvis 2020). The fourth column contains the average CT_{index} values during the event intervals. Extinction rates after Kocsis *et al.* (2019) are proportionally normalised to a range of 0 to 1, the sixth column is derived from the method ‘sqs2f3’. ER_Diff_Min. and Max. represent the minimum and maximum values under all the ER calculation methods in Kocsis *et al.* (2019), respectively. ER_error_bar_N. = (ER_sqs2f3 - ER_Diff_Min.), ER_error_bar_P. = (ER_Diff_Max - ER_sqs2f3.) Neg. = negative, Pos. = positive. ER of different phylum is derived from the method ‘sqs2f3’.

| Events | Age (Ma) | Stages | CT_index (%) | CT_error bar | ER_sqs2f3 (normalised) | ER_Diff | | ER_error_bar | | Extinction_rate_different_phylum | | | | | | |
|------------------|-----------------|--------------------------------|--------------|--------------|------------------------|---------|------|--------------|------|----------------------------------|-------------|-------------|------------|----------|------------|--|
| | | | | | | Min. | Max. | Neg. | Pos. | Cnidaria | Brachiopoda | Cephalopoda | Arthropoda | Bivalvia | Gastropoda | |
| 1900 - 2100 A.D. | | After Suess effect | 0.4 - 1.5 | 0.06 | | | | | | | | | | | | |
| 750 - 1900 A.D. | | Before Suess effect | < 0.1 | 0.06 | | | | | | | | | | | | |
| 0 - 0.0117 Ma | | Holocene | 0.23 | 0.06 | | | | | | | | | | | | |
| Pli | 2.6 - 3.6 | Late Pliocene | 0.11 | 0.06 | 0.19 | 0.10 | 0.32 | 0.09 | 0.14 | 0.16 | 0.06 | | 0.19 | 0.12 | 0.18 | |
| B. Tor | 9 - 10 | Tortonian | 0.04 | 0.06 | 0.02 | 0.02 | 0.13 | 0.00 | 0.11 | 0.10 | -0.01 | | 0.16 | 0.00 | -0.03 | |
| B. Lan | 13.8 - 13.9 | Langhian | 0.03 | 0.06 | 0.05 | 0.00 | 0.12 | 0.05 | 0.07 | 0.00 | 0.07 | | 0.08 | 0.01 | 0.06 | |
| PrOM | 36.6 - 36.7 | Priabonian | 0.12 | 0.06 | 0.14 | 0.06 | 0.18 | 0.08 | 0.05 | 0.11 | 0.29 | | 0.35 | 0.08 | 0.11 | |
| B. ETM2 | 53.54 - 53.62 | Ypresian | 0.10 | 0.06 | 0.05 | 0.03 | 0.09 | 0.01 | 0.05 | 0.07 | 0.09 | 0.00 | 0.26 | 0.02 | -0.01 | |
| PETM | 55.73 - 56.01 | Thanetian - Ypresian Tran. | 0.33 | 0.06 | 0.07 | 0.06 | 0.20 | 0.01 | 0.13 | 0.12 | 0.26 | 0.06 | 0.01 | 0.01 | 0.06 | |
| KPg | 65.975 - 66.0 | Maastrichtian - Danian Tran. | 0.13 | 0.06 | 0.28 | 0.13 | 0.41 | 0.15 | 0.13 | 0.34 | 0.34 | | 0.14 | 0.35 | 0.22 | |
| OAE2 | 94.46 - 94.54 | Cenomanian-Turonian Tran. | 0.26 | 0.06 | 0.22 | 0.06 | 0.31 | 0.16 | 0.09 | 0.24 | 0.43 | 0.47 | 0.21 | 0.11 | 0.10 | |
| OAE1a | 120.1 - 120.2 | Aptian | 0.19 | 0.06 | 0.19 | 0.07 | 0.27 | 0.13 | 0.08 | 0.10 | 0.12 | 0.25 | 0.13 | 0.06 | 0.05 | |
| Kim | 149.8 - 149.86 | Late Kimmeridgian | 0.14 | 0.06 | 0.15 | 0.06 | 0.22 | 0.09 | 0.07 | 0.01 | 0.36 | 0.31 | 0.39 | 0.10 | 0.11 | |
| PToBE & TOAE | 182 - 185 | Pliensbachian - Toarcian Tran. | 0.24 | 0.06 | 0.19 | 0.05 | 0.22 | 0.14 | 0.03 | 0.44 | 0.27 | 0.39 | 0.01 | 0.09 | 0.13 | |
| TJ | 201.25 - 201.3 | Rhaetian - Hettangian Tran. | 1.02 | 0.06 | 0.51 | 0.18 | 0.69 | 0.33 | 0.18 | 0.65 | 0.30 | 0.99 | 0.27 | 0.14 | 0.24 | |
| Nor | 215.62 - 215.74 | Norian | 0.40 | 0.06 | 0.28 | 0.10 | 0.34 | 0.18 | 0.06 | 0.17 | 0.32 | 0.35 | -0.05 | 0.25 | 0.18 | |
| CPE | 234.4 - 234.46 | Mid - Carnian | 0.22 | 0.06 | 0.20 | 0.13 | 0.29 | 0.08 | 0.09 | 0.17 | 0.31 | 0.31 | 0.20 | 0.06 | 0.11 | |
| B. An | 242 - 243 | Late Anisian | 0.02 | 0.06 | 0.02 | 0.01 | 0.11 | 0.02 | 0.09 | | 0.01 | 0.11 | 0.08 | 0.06 | 0.01 | |



| | | | | | | | | | | | | | | | |
|--------------|------------------|------------------------------|------|------|------|------|------|------|------|------|-------|-------|-------|-------|-------|
| Ind | 251.42 - 251.52 | Induan | 0.39 | 0.06 | 0.26 | 0.07 | 0.40 | 0.19 | 0.14 | | | -0.02 | 0.06 | 0.04 | 0.12 |
| PTr | 251.941 - 251.88 | Changhsingian - Induan Tran. | 1.16 | 0.06 | 0.81 | 0.34 | 0.89 | 0.47 | 0.08 | | 0.95 | 0.63 | 0.26 | 0.74 | 0.57 |
| Cap | 260.5 - 261 | Mid - Capitanian | 0.51 | 0.06 | 0.20 | 0.13 | 0.27 | 0.07 | 0.07 | 0.16 | 0.17 | 0.34 | 0.08 | 0.15 | 0.07 |
| B_Sak | 291.5 - 292.5 | Sakmarian | 0.05 | 0.06 | 0.01 | 0.01 | 0.11 | 0.00 | 0.11 | 0.07 | 0.00 | 0.24 | -0.09 | -0.03 | 0.01 |
| B_Gzh | 300 - 301 | Gzhelian | 0.03 | 0.06 | 0.05 | 0.03 | 0.15 | 0.02 | 0.11 | 0.06 | -0.01 | 0.15 | 0.06 | -0.08 | 0.13 |
| VS | 335.5 - 335.7 | Visean - Serpukhovian Tran. | 0.31 | 0.06 | 0.22 | 0.09 | 0.34 | 0.13 | 0.11 | 0.25 | 0.14 | 0.24 | 0.40 | 0.05 | 0.07 |
| Hangenberg | 359.2 - 359.7 | Famennian - Tourisian Tran. | 0.62 | 0.06 | 0.38 | 0.14 | 0.40 | 0.24 | 0.02 | 0.43 | 0.36 | 0.36 | 0.32 | 0.16 | 0.19 |
| FF | 375 - 372 | Frasnian | 0.20 | 0.06 | 0.16 | 0.12 | 0.35 | 0.04 | 0.19 | 0.37 | 0.13 | 0.13 | 0.14 | 0.12 | 0.04 |
| GF | 379 - 380 | Givetian - Frasnian Tran. | 0.43 | 0.06 | 0.23 | 0.16 | 0.33 | 0.07 | 0.10 | 0.44 | 0.13 | 0.34 | 0.41 | 0.07 | 0.14 |
| Pri | 419 - 419.5 | Late Pridoli | 0.22 | 0.06 | 0.13 | 0.09 | 0.19 | 0.05 | 0.06 | 0.04 | 0.13 | 0.02 | 0.15 | 0.15 | 0.02 |
| Sil_Lau | 423.1 - 423.5 | Ludfordian | 0.68 | 0.06 | 0.05 | 0.02 | 0.09 | 0.02 | 0.05 | 0.01 | 0.05 | 0.02 | 0.03 | 0.05 | 0.08 |
| Sil_Mulde | 427.66 - 428.32 | Homerian | 0.66 | 0.06 | 0.07 | 0.06 | 0.16 | 0.02 | 0.09 | 0.02 | 0.11 | | 0.14 | 0.04 | -0.03 |
| Sil_Ireviken | 431.72 - 431.84 | Sheinwoodian | 0.61 | 0.06 | 0.10 | 0.07 | 0.14 | 0.02 | 0.04 | 0.10 | 0.08 | | 0.03 | 0.16 | 0.00 |
| B_Rhu | 441 - 443 | Rhuddanian | 0.11 | 0.06 | 0.05 | 0.05 | 0.16 | 0.00 | 0.11 | 0.03 | 0.14 | -0.03 | 0.15 | 0.01 | 0.00 |
| Ord_2 | 444.56 - 444.74 | Hirntian | 0.48 | 0.06 | 0.23 | 0.13 | 0.37 | 0.10 | 0.14 | 0.14 | 0.06 | 0.29 | 0.27 | 0.14 | 0.19 |
| Ord_1 | 452.42 - 452.48 | Early Katian | 0.60 | 0.06 | 0.40 | 0.16 | 0.48 | 0.24 | 0.09 | 0.28 | 0.28 | 0.28 | 0.35 | 0.10 | 0.15 |
| B_Dar | 460 - 465 | Darriwilian | 0.02 | 0.06 | 0.04 | 0.00 | 0.22 | 0.04 | 0.18 | | 0.14 | 0.01 | 0.13 | -0.01 | 0.09 |
| TSICE | 481.9 - 482.5 | Tremadocian | 0.28 | 0.06 | 0.59 | 0.39 | 0.64 | 0.20 | 0.05 | | 0.47 | 0.53 | 0.81 | | 0.59 |
| JiangS | 494.2 - 494.4 | Paibian - Jiangshanian Tran. | 0.15 | 0.06 | 0.44 | 0.23 | 0.61 | 0.22 | 0.16 | | 0.22 | | 0.73 | | |
| SPICE | 496.42 - 496.5 | Paibian | 0.17 | 0.06 | 0.12 | 0.11 | 0.26 | 0.01 | 0.14 | | 0.06 | | 0.08 | | |
| Cam_7 | 497.1 - 497.2 | Late Guzhangian | 0.12 | 0.06 | 0.64 | 0.32 | 0.90 | 0.31 | 0.26 | | 0.61 | | 0.97 | | |
| Cam_6 | 503.7 - 504.2 | Drumian | 0.12 | 0.06 | 0.69 | 0.30 | 0.75 | 0.40 | 0.06 | | 0.16 | | 0.81 | | |
| Cam_5 | 508.7 - 508.9 | Wulian | 0.13 | 0.06 | 0.45 | 0.31 | 0.57 | 0.14 | 0.12 | | 0.19 | | 0.87 | | |
| Cam_4 | 514.12 - 514.34 | Cambrian Age 4 | 0.14 | 0.06 | 0.47 | 0.39 | 0.63 | 0.08 | 0.16 | | 0.46 | | 0.14 | | |
| Cam_3 | 517.82 - 518 | Cambrian Age 3 | 0.18 | 0.06 | 0.36 | 0.21 | 0.39 | 0.15 | 0.03 | | 0.42 | | | | |
| Cam_2 | 521 - 529 | Cambrian Age 2 | 0.41 | 0.06 | 0.19 | 0.18 | 0.34 | 0.01 | 0.15 | | 0.19 | | | | |



Supplementary Figures

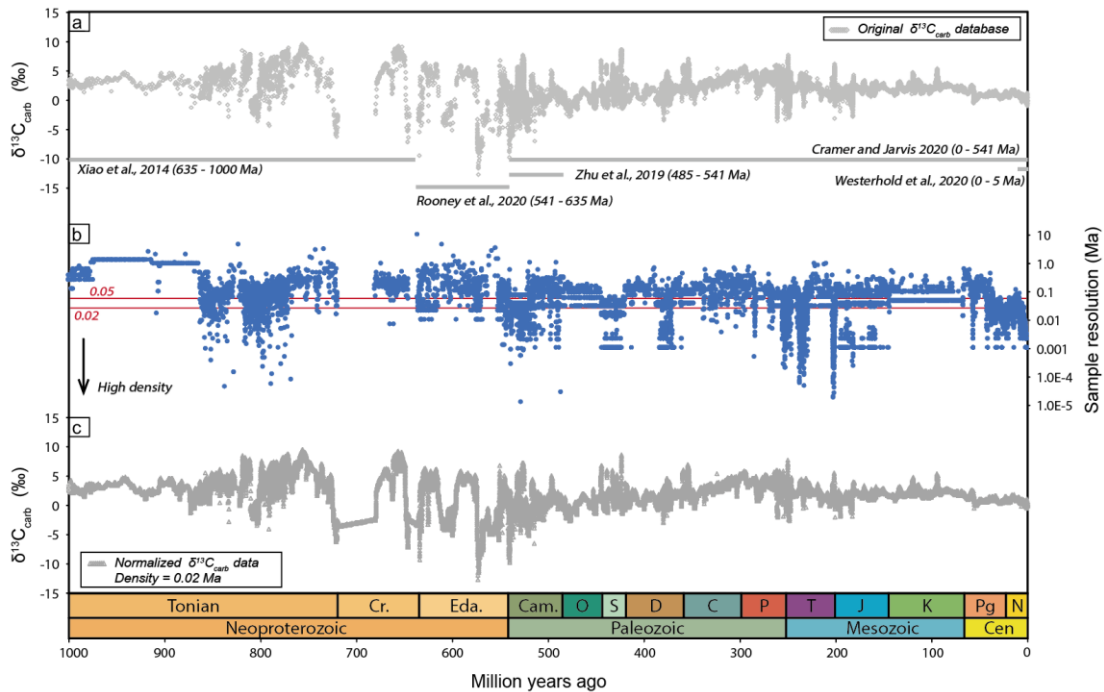


Figure S-1 (a) Variation in $\delta^{13}\text{C}_{\text{carb}}$ through the last 1 billion years. Data sources are indicated by lateral bars showing chronostratigraphic intervals. (b) Sample resolution over the one-billion-year interval. (c) The normalised $\delta^{13}\text{C}_{\text{carb}}$ dataset, where the function ‘interp1’ with method ‘Linear’ in Matlab was used to uniformly change the data density to 0.02 Ma.

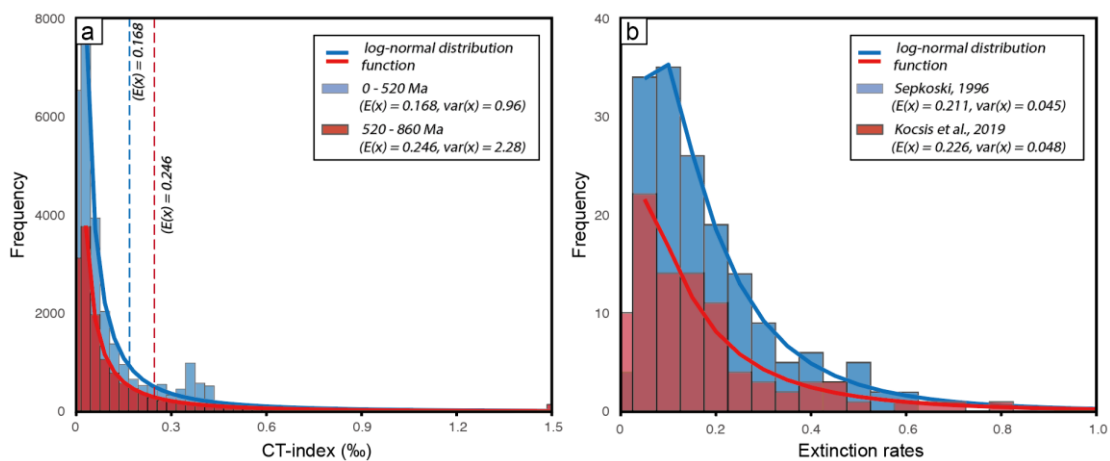


Figure S-2 Histograms and best fit curves of the log-normal function relative to: a. CT_{index} values (0 to 1000 Ma); b. calculated extinction rates (Sepkoski, 1996; Kocsis *et al.*, 2019). $E(x)$ and $\text{var}(x)$ represent the mathematical expectation and variation of the dataset x , respectively.

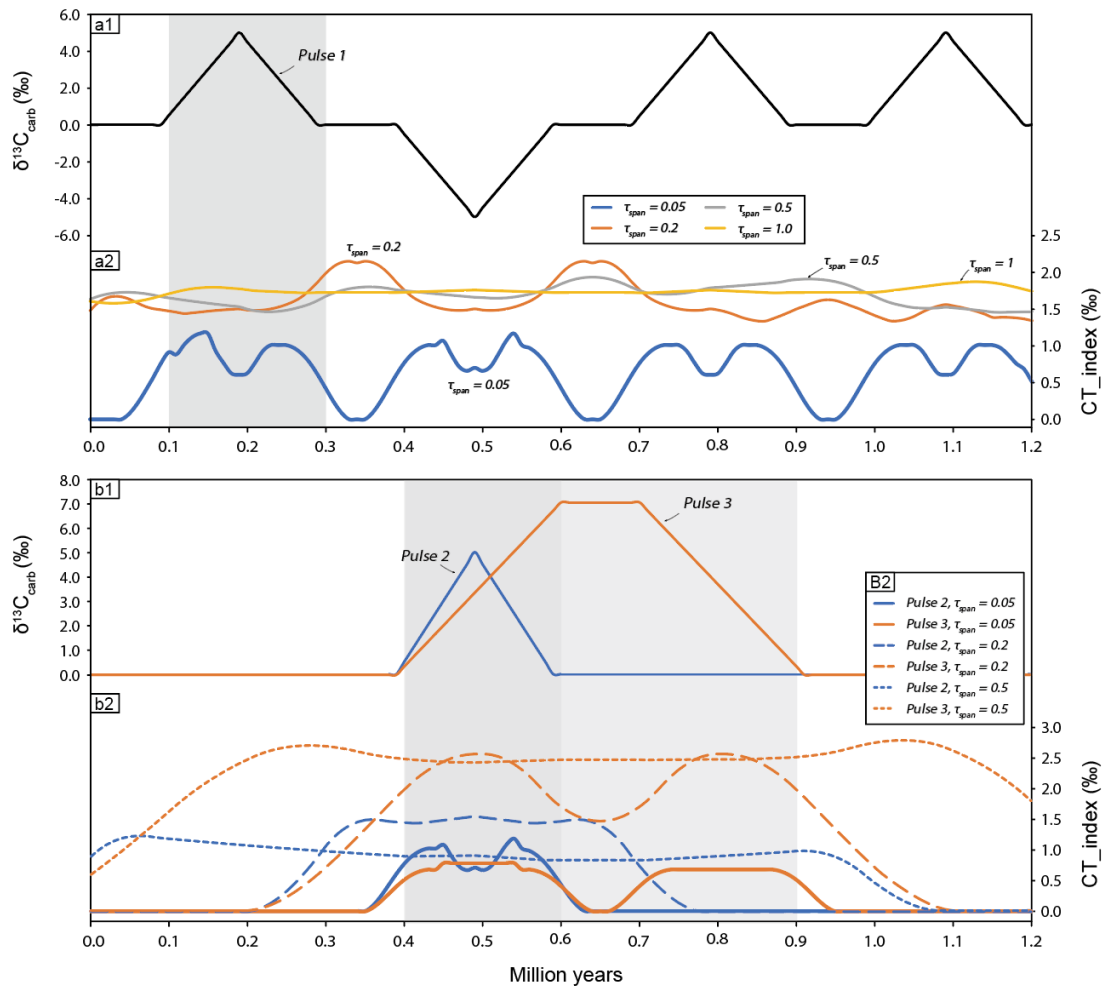


Figure S-3 Sensitivity test for parameter τ_{span} . **(a1-2)** Pulse 1 with four different τ_{span} values (0.05, 0.2, 0.5, 1 Ma). The CT_{index} is not sensitive to the direction of the carbon isotope excursions, and a longer τ_{span} obscures individual events and gives unrealistically high CT_{index} values. **(b1-2)** Pulse 2 and 3, with three different τ_{span} values (0.05, 0.2, 0.5 Ma). The relationship between the duration of the events and the τ_{span} has a profound effect on calculated CT_{index} values.

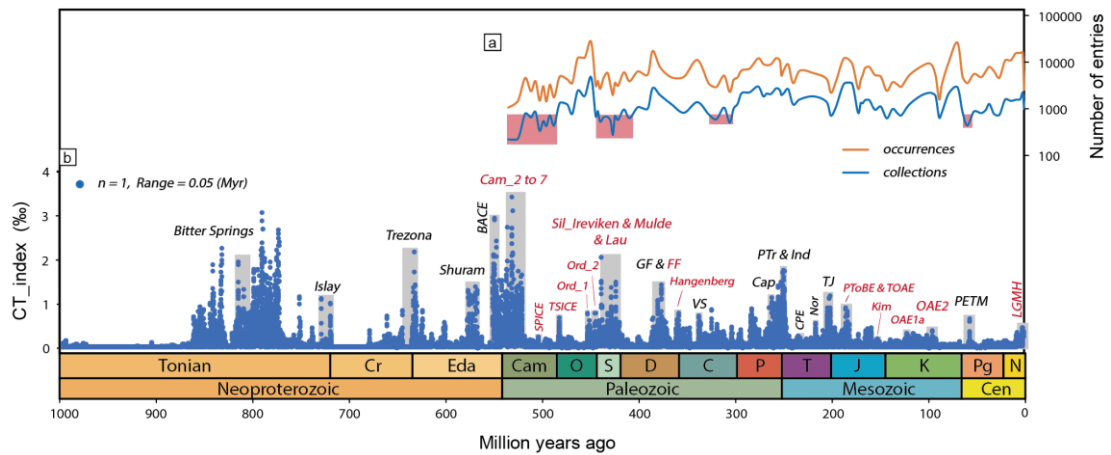


Figure S-4 (a) Occurrences and collections of the Paleobiology database through the Phanerozoic. The red boxes represent the period with extremely low collections including: Cambrian, the Silurian, and stages Bashkirian, Kasimovian and Thanetian. **(b)** CT_{index} peaks and their correspondent $\delta^{13}\text{C}_{\text{carb}}$ events over the last 1,000 Myr. All CT_{index} peaks correspond to extreme $\delta^{13}\text{C}_{\text{carb}}$ events, documenting either positive or negative excursions. See Table S-2 for event names. Black and red marks represent negative and positive $\delta^{13}\text{C}_{\text{carb}}$ excursions, respectively.

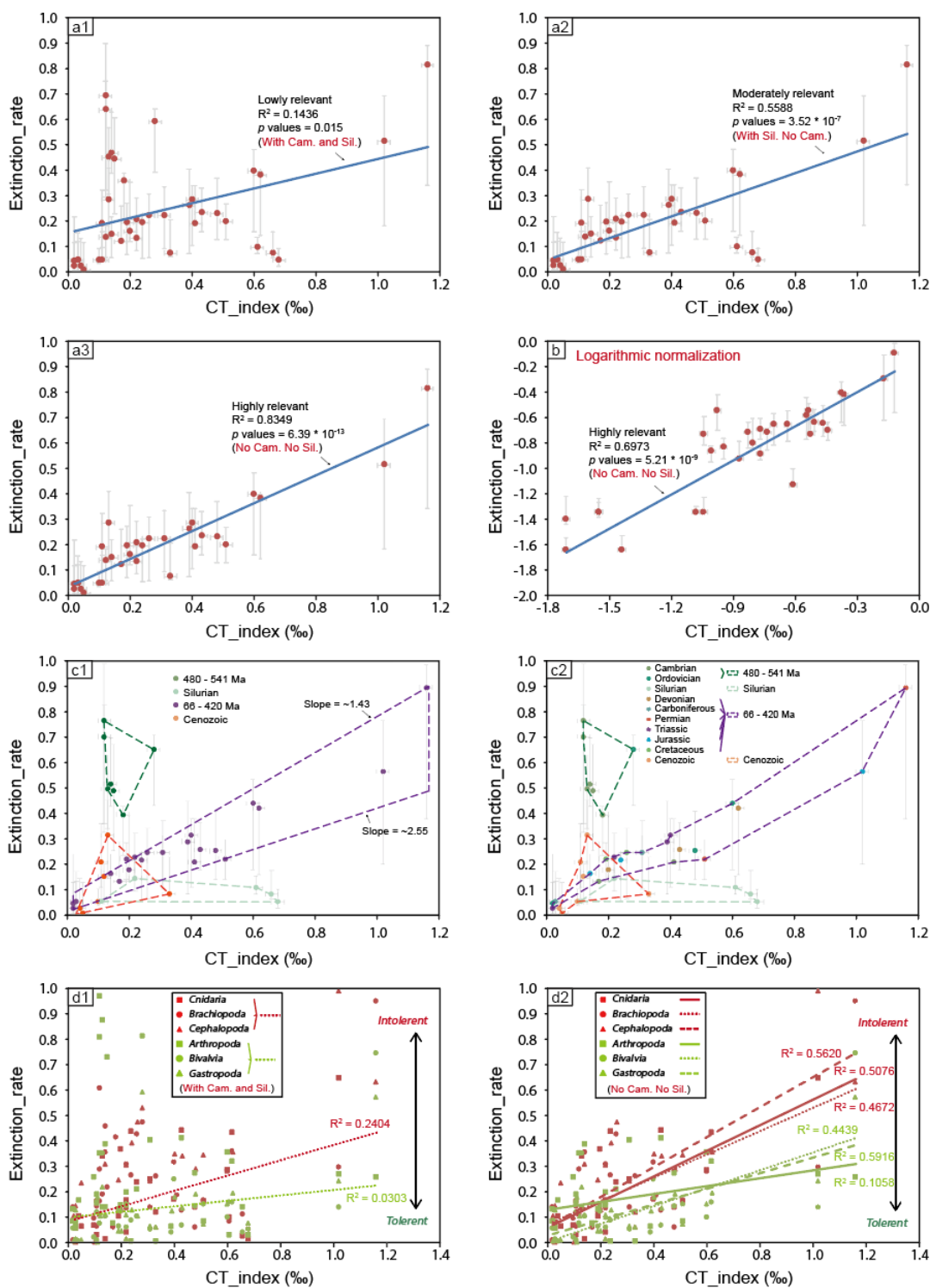


Figure S-5 Cross-plots of the CT_{index} and ER, and their correlations **(a1)** with Cambrian and Silurian data, **(a2)** with Silurian and without Cambrian data, and **(a3)** without Cambrian and Silurian data. **(b)** The CT_{index} and ER values are logarithmic normalised to eliminate the effect of order of magnitude differences in correlation. This accounts for the effect of extremely high values during the PTR and TJ. **(c1-2)** Cross-plots of the CT_{index} and ER for different time intervals. Nearly all the data points fall within the purple zones, with the exception of the Cambrian, Silurian and Cenozoic. **(d1-**

2) Cross-plots of the CT_{index} and ER for different phyla. The higher the ER/ CT_{index} slope, the more intolerant the phylum was during the extinction events.

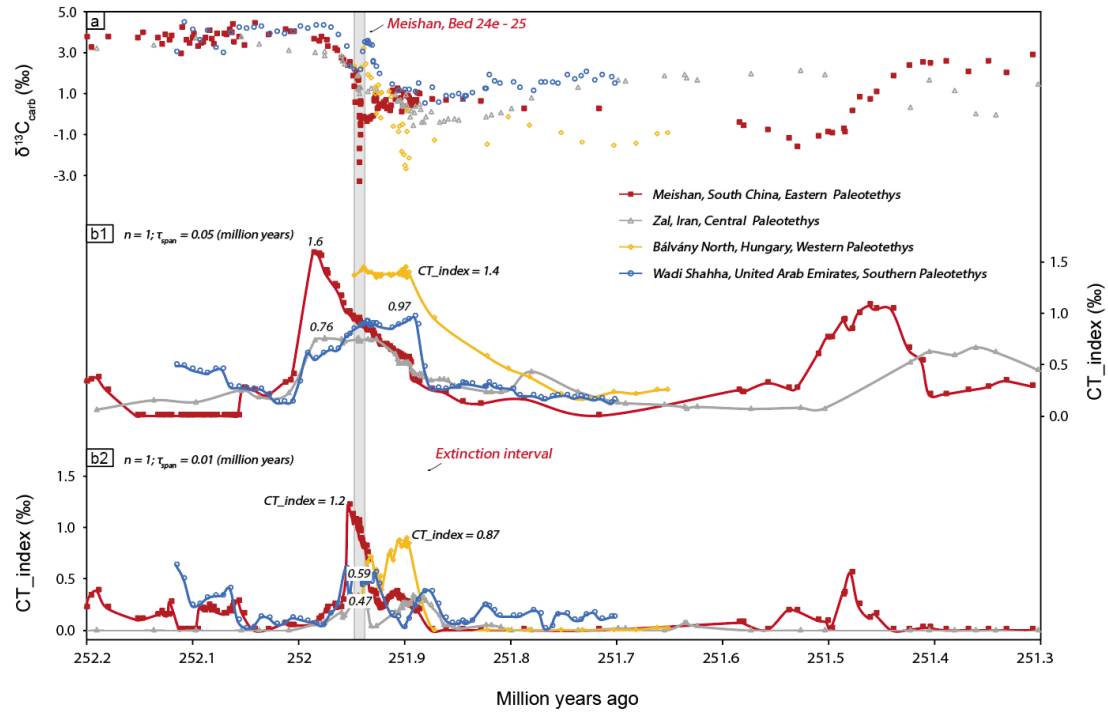


Figure S-6 (a) $\delta^{13}C_{carb}$ data for the Permian-Triassic transition from 252.2 to 251.3 Ma. Data sources: Meishan (Burgess *et al.*, 2014), Zal (Zhang *et al.*, 2018), Bálvány North (Schobben *et al.*, 2017), Wadi Shahha (Clarkson *et al.*, 2013). **(b1-2)** CT_{index} for the $\delta^{13}CO_2$ curves, where parameter $n = 1$, and r was set equal to 0.05 **(b1)** and 0.01 **(b2)**.

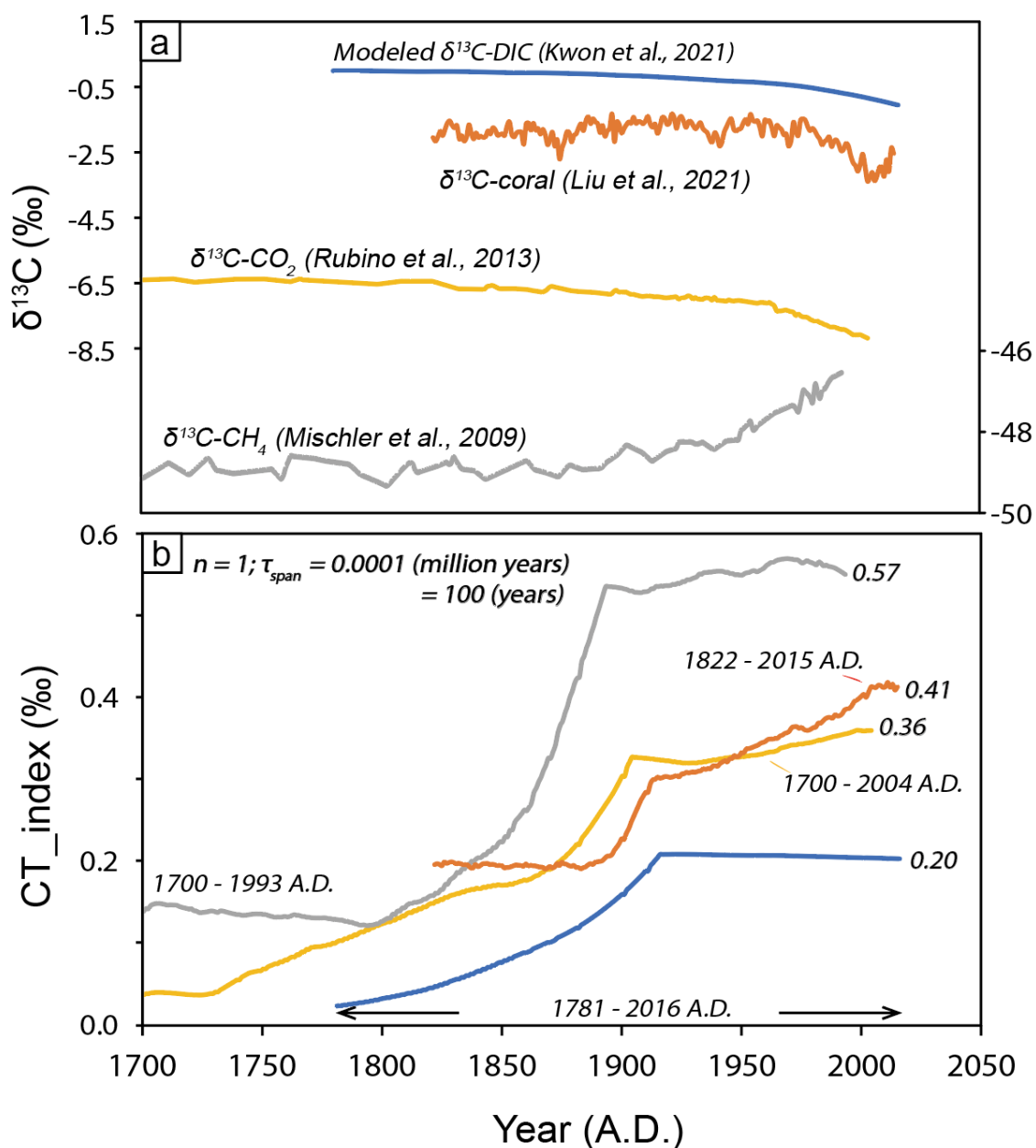


Figure S-7 (a) Carbon isotope trajectories for ocean surface dissolved inorganic carbon (DIC), coral from the northern South China sea, CO₂ from air bubbles trapped in continental ice, and CH₄ in Antarctica ice core. **(b)** Calculated CT_{index} for these datasets. Data sources, the time interval of each dataset, and the CT_{index} values are marked on the figure.

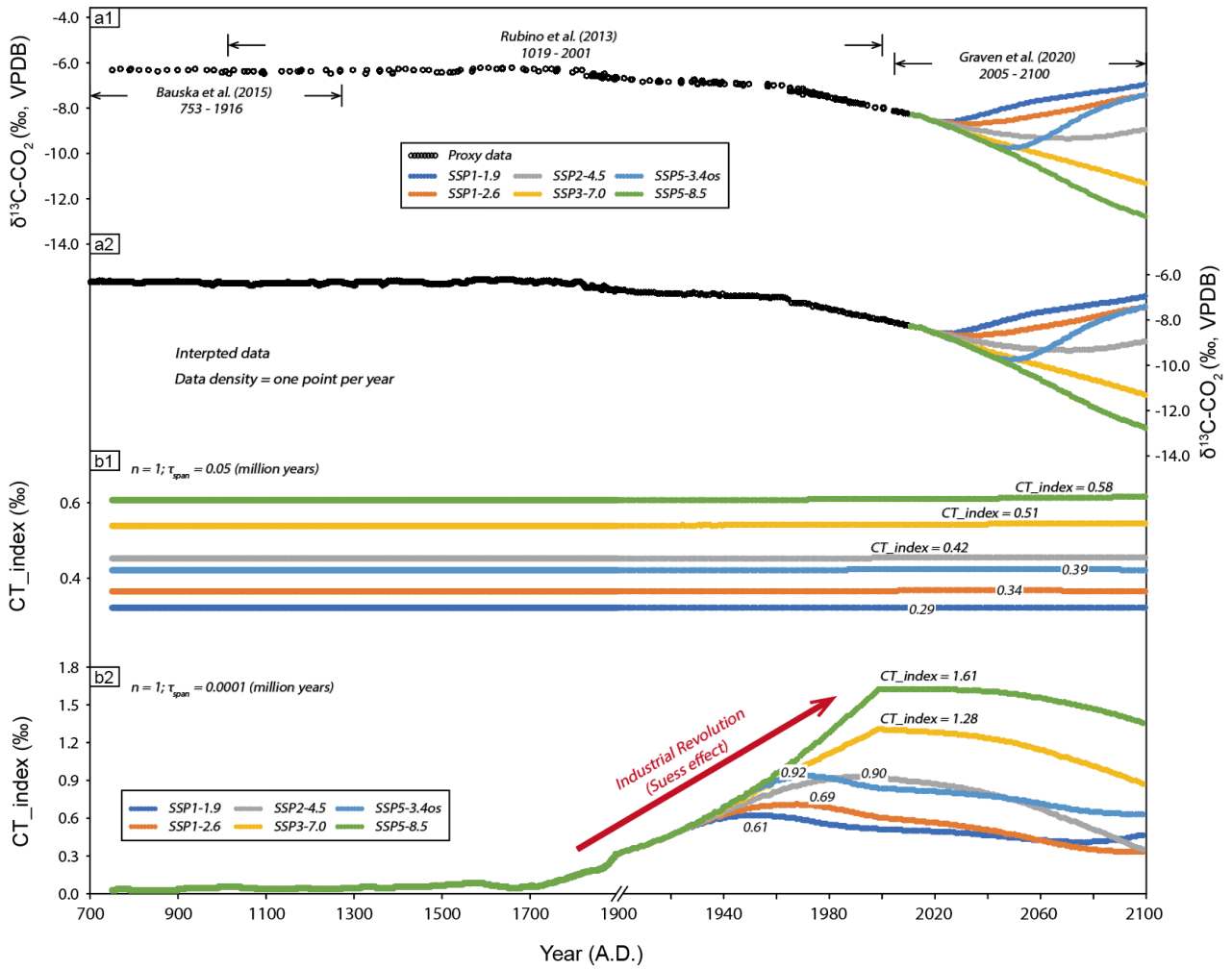


Figure S-8 (a) Observed $\delta^{13}\text{CO}_2$ for 750 to 2015 A.D., and simulated $\delta^{13}\text{CO}_2$ for 2015 to 2100 A.D. for the six SSP-based CMIP6 ScenarioMIP scenarios (after Graven *et al.*, 2020). Data sources are indicated by lateral bars. **(b1-2)** CT_{index} of the $\delta^{13}\text{CO}_2$ curves, where parameter $n = 1$, and r was set equal to 0.05 **(b1)** and 0.0001 **(b2)**, respectively. A.D. = Anno Domini.

Supplementary Information References

- Bachan, A., Lau, K. V., Saltzman, M.R., Thomas, E., Kump, L.R., Payne, J.L. (2017) American journal of science: A model for the decrease in amplitude of carbon isotope excursions across the phanerozoic. *American Journal of Science* 317, 641–676.
- Bauska, T.K., Joos, F., Mix, A.C., Roth, R., Ahn, J., Brook, E.J. (2015) Links between atmospheric carbon dioxide, the land carbon reservoir and climate over the past millennium. *Nature Geoscience* 8, 383–387.
- Burgess, S.D., Bowring, S., Shen, S.Z. (2014) High-precision timeline for Earth's most severe extinction. *Proceedings of the National Academy of Sciences of the United States of America* 111, 3316–3321.
- Clarkson, M.O., Richoz, S., Wood, R.A., Maurer, F., Krystyn, L., McGurty, D.J., Astratti, D. (2013) A new high-resolution $\delta^{13}\text{C}$ record for the Early Triassic: Insights from the Arabian Platform. *Gondwana Research*. International Association for Gondwana Research 24, 233–242.
- Cramer, B.D., Jarvis, I. (2020) Chapter 11 - Carbon Isotope Stratigraphy. In: Gradstein, F.M., Ogg, J.G., Schmitz, M.D., Ogg, G.M. (Eds.) *The Geologic Time Scale 2020*. Elsevier, Amsterdam, 309–343, doi: 10.1016/B978-0-12-824360-2.00011-5.
- Fan, J.X., Shen, S.Z., Erwin, D.H., Sadler, P.M., Macleod, N., Cheng, Q.M., Hou, X.D., Yang, J., Wang, X.D., Wang, Y., Zhang, H., Chen, X., Li, G.X., Zhang, Y.C., Shi, Y.K., Yuan, D.X., Chen, Q., Zhang, L.N., Li, C., Zhao, Y.Y. (2020) A high-resolution summary of Cambrian to Early Triassic marine invertebrate biodiversity. *Science* 367, 272–277.
- Graven, H., Keeling, R.F., Rogelj, J. (2020) Changes to Carbon Isotopes in Atmospheric CO₂ Over the Industrial Era and Into the Future. *Global Biogeochemical Cycles* 34, 1–21.
- Knoll, A.H., Bambach, R.K., Payne, J.L., Pruss, S., Fischer, W.W. (2007) Paleophysiology and end-Permian mass extinction. *Earth and Planetary Science Letters* 256, 295–313.
- Kocsis, A.T., Reddin, C.J., Alroy, J., Kiessling, W. (2019) The r package divDyn for quantifying diversity dynamics using fossil sampling data. *Methods in Ecology and Evolution* 10, 735–743.
- Kwon, E.Y., DeVries, T., Galbraith, E.D., Hwang, J., Kim, G., Timmermann, A. (2021) Stable Carbon Isotopes Suggest Large Terrestrial Carbon Inputs to the Global Ocean. *Global Biogeochemical Cycles* 35, 1–25.
- Liu, X., Deng, W., Cui, H., Chen, X., Cai, G., Zeng, T., Wei, G. (2021) Change of coral carbon isotopic response to anthropogenic Suess effect since around 2000s. *Marine Environmental Research* 168, 105328.



- Mischler, J.A., Sowers, T.A., Alley, R.B., Battle, M., McConnell, J.R., Mitchell, L., Popp, T., Sofen, E., Spencer, M.K. (2009) Carbon and hydrogen isotopic composition of methane over the last 1000 years. *Global Biogeochemical Cycles* 23, 1–13.
- Payne, J.L., Bachan, A., Heim, N.A., Hull, P.M., Knope, M.L. (2020) The evolution of complex life and the stabilization of the Earth system. *Interface Focus* 10, 20190106.
- Rothman, D.H. (2017) Thresholds of catastrophe in the Earth system. *Science Advances* 3, e1700906.
- Rooney, A.D., Cantine, M.D., Bergmann, K.D., Gómez-Pérez, I., Baloushi, B. Al, Boag, T.H., Busch, J.F., Sperling, E.A., Strauss, J.V. (2020) Calibrating the coevolution of Ediacaran life and environment. *Proceedings of the National Academy of Sciences of the United States of America* 117, 16824–16830.
- Rubino, M., Etheridge, D.M., Trudinger, C.M., Allison, C.E., Battle, M.O., Langenfelds, R.L., Steele, L.P., Curran, M., Bender, M., White, J.W.C., Jenk, T.M., Blunier, T., Francey, R.J. (2013) A revised 1000 year atmospheric $\delta^{13}\text{C-CO}_2$ record from Law Dome and South Pole, Antarctica. *Journal of Geophysical Research Atmospheres* 118, 8482–8499.
- Schobben, M., Stebbins, A., Algeo, T.J., Strauss, H., Leda, L., Haas, J., Struck, U., Korn, D., Korte, C. (2017) Volatile earliest Triassic sulfur cycle: A consequence of persistent low seawater sulfate concentrations and a high sulfur cycle turnover rate? *Palaeogeography, Palaeoclimatology, Palaeoecology* 486, 74–85.
- Sepkoski, J.J. (1996) Patterns of Phanerozoic Extinction: a Perspective from Global Data Bases. *Global Events and Event Stratigraphy in the Phanerozoic* 35–51.
- Suess, H.E. (1955) Radiocarbon concentration in modern wood. *Science* 122, 415–417.
- Swart, P.K. (2008) Global synchronous changes in the carbon isotopic composition of carbonate sediments unrelated to changes in the global carbon cycle. *Proceedings of the National Academy of Sciences of the United States of America* 105, 13741–13745.
- Westerhold, T., Marwan, N., Drury, A.J., Liebrand, D., Agnini, C., Anagnostou, E., Barnet, J.S.K., Bohaty, S.M., Vleeschouwer, D.D., Florindo, F., Frederichs, T., Hodell, D.A., Holbourn, A.E., Kroon, D., Laurentano, V., Littler, K., Lourens, L.J., Lyle, M., Palike, H., Rohl, U., Tian, J., Wilkens, R.H., Wilson, P.A., Zachos, J. (2020) An astronomically dated record of Earth's climate and its predictability over the last 66 million years. *Science* 369, 1383–1388.
- Xiao, S., Shen, B., Tang, Q., Kaufman, A.J., Yuan, X., Li, J., Qian, M. (2014) Biostratigraphic and chemostratigraphic constraints on the age of early Neoproterozoic carbonate successions in North China. *Precambrian Research*, 246, 208–225.



- Zhang, F.F., Romaniello, S.J., Algeo, T.J., Lau, K.V., Clapham, M.E., Richoz, S., Herrmann, A.D., Smith, H., Horacek, M., Anbar, A.D. (2018) Multiple episodes of extensive marine anoxia linked to global warming and continental weathering following the latest Permian mass extinction. *Science Advances* 4, e1602921.
- Zhu, M., Yang, A., Yuan, J., Li, G., Zhang, J., Zhao, F., Ahn, S.Y., Miao, L. (2019) Cambrian integrative stratigraphy and timescale of China. *Science China Earth Sciences* 62, 25–60.

